Interdisciplinary Research in Medical Sciences Specialty
ISSN: 3062-4401
2025, Volume 5, Issue 2, Page No: 187-202

Available online at: www.galaxypub.co/page/journals

Galaxy Publication

Riemannian Clustering-Based Decoding of Lower Limb Motor Imagery EEG Signals for Brain–Computer Interfaces

Youssef Hariri[1]*, Hassan Nasser[1], Fatima Zahra[2]

[1]Department of Brain–Computer Interfaces and Signal Processing, Faculty of Medicine, Mohammed V University, Rabat, Morocco.
[2]Department of Motor Imagery and EEG Analysis, Faculty of Medicine, University of Casablanca, Casablanca, Morocco.

***E-mail** ✉ youssef.hariri@um5.ac.ma

Received: 22 July 2025; **Revised:** 28 September 2025; **Accepted:** 05 October 2025

ABSTRACT

Brain-computer interfaces (BCIs) utilizing motor imagery (MI) have emerged as a promising rehabilitation strategy for individuals recovering from stroke. Classification techniques founded on Riemannian geometry are commonly adopted in MI-BCI systems because of their exceptional robustness and capacity for generalization. Nonetheless, existing algorithms exhibit limitations in clustering performance, primarily due to clustering criteria that are inadequately adapted to the specific characteristics of lower-limb electroencephalography (EEG) signals. To overcome this challenge, the current investigation introduces two novel classification approaches based on Riemannian clustering: margin-based Riemannian clusters (MBRC) and statistics-based Riemannian clusters (SBRC). These methods segment the complete set of samples into subclusters using Riemannian distance measures and introduce original clustering standards. Cluster margin distance and the Riemannian potato algorithm were adopted as the new criteria to enable more reliable classification of lower-limb MI-EEG data. Evaluation of MBRC and SBRC was conducted on both an in-house experimental dataset and the publicly accessible Yi2014 dataset. Results from the experimental dataset revealed average classification accuracies of 71.29% for MBRC and 73.12% for SBRC, exceeding the performance of baseline methods. On the Yi2014 dataset, the proposed algorithms consistently surpassed comparative techniques across different training sample sizes, demonstrating particular advantages under conditions of limited data availability. Overall, these outcomes highlight the enhanced suitability of the developed algorithms for accurate classification of lower-limb MI-EEG signals.

Keywords: Brain-computer interface (BCI), Motor imagery (MI), Riemannian clustering, Subcluster

How to Cite This Article: Hariri Y, Nasser H, Zahra F. Riemannian Clustering-Based Decoding of Lower Limb Motor Imagery EEG Signals for Brain–Computer Interfaces. Interdiscip Res Med Sci Spec. 2025;5(2):187-202. https://doi.org/10.51847/lcfmKotbWy

Introduction

Following a stroke, over 85% of patients suffer from motor impairments, among which lower-limb hemiplegia constitutes a frequent and debilitating deficit [1]. Conventional rehabilitation approaches for restoring lower-limb function typically rely on active and passive exercises targeting the distal extremities to indirectly activate central neural pathways. However, these interventions often underutilize the patient's voluntary motor intentions, thereby constraining the overall effectiveness of neural reorganization [2]. As a result, substantial research attention has shifted toward the creation of advanced rehabilitation modalities. Brain-computer interfaces (BCIs) represent one such promising technology. A BCI functions as a specialized system that supports direct, bidirectional communication between the brain and external devices [3]. These systems encompass multiple operational paradigms, such as P300 event-related potentials [4], steady-state visual evoked potentials [5], and motor imagery (MI) [6]. MI-BCI, in particular, offers significant potential across various domains by enabling users to engage with their surroundings through intuitive mental processes [7].

Accurate processing of MI-EEG signals forms a critical foundation for successful MI-BCI deployment. Such signals harbor distinctive features useful for differentiating MI tasks, including the motor-related cortical potential (MRCP) and sensorimotor rhythm (SMR) [8, 9]. Yet, MRCP signals elicited by motor imagery tend to be less pronounced than those generated during physical movement execution [10]. Moreover, their reliable extraction necessitates precise temporal alignment, which limits their practical utility in MI-EEG classification tasks. SMR, by comparison, comprises Mu and Beta frequency bands originating in the sensorimotor cortical areas [11]. This rhythm undergoes modulation in response to actual or imagined movements, manifesting as a reduction in amplitude known as event-related desynchronization (ERD) [6]. ERD is characteristically detectable in the hemisphere contralateral to the imagined movement, for example during left- or right-hand motor imagery [12]. Consequently, MI-BCI systems can decode intended actions by capturing the spatial distribution of ERD patterns across sensorimotor regions [13].

Contemporary MI-BCI algorithms fall into three primary categories [14]: traditional filtering methods, deep learning techniques, and Riemannian geometry approaches. Filtering-based strategies focus on extracting temporal and spatial EEG features for subsequent identification. The common spatial pattern (CSP) algorithm is particularly prevalent in this category due to its straightforward implementation and computational advantages [15]. Its effectiveness, however, is heavily influenced by the choice of frequency bands. To address this constraint, several refined CSP variants have been developed that incorporate optimized band selection procedures [16–18]. Deep learning frameworks excel at automatically identifying the most discriminative features embedded within EEG recordings, leading to improved classification outcomes [19, 20]. Riemannian geometry methods, on the other hand, transform EEG covariance matrices onto a Riemannian manifold. This mathematical framework confers inherent resilience to noise contamination and strong generalization properties [21].

Signals associated with lower-limb motor intentions are especially susceptible to contamination by multiple artifact sources, including electromagnetic interference and movement-related noise. Effective classification in this context therefore demands algorithms with superior noise tolerance and robust outlier handling. Riemannian geometry-based techniques are especially advantageous for lower-limb EEG classification under such conditions. Cluster analysis performed via Riemannian distance metrics constitutes a key application area within this class of algorithms. The minimum distance to mean (MDM) approach introduced by Barachant continues to be the predominant Riemannian manifold classifier, partly because of the limited availability of appropriate unsupervised manifold learning alternatives [22, 23]. In light of this, the present study advances an improved manifold-compatible clustering algorithm. The concept of subclustering is employed to partition each primary class into several finer subclusters, thereby increasing intra-cluster coherence. Implementation of this strategy involves assigning both a sample status indicator and a class status indicator to each data point.

Clustering criteria are commonly grouped into distance-based, density-based, and linkage-based families. Although the first two are generally restricted to Euclidean spaces, linkage-based methods extend naturally to arbitrary metric spaces [24]. Given the inherent complexity of lower-limb MI-EEG discrimination and the prevalence of artifacts, a single criterion proves insufficient for reliable subcluster identification. Therefore, two distinct classification strategies were developed: one grounded in large-margin principles and the other utilizing the Riemannian potato algorithm. These are designated as margin-based Riemannian clusters (MBRC) and statistics-based Riemannian clusters (SBRC). MBRC strengthens discrimination at class boundaries and elevates overall clustering fidelity. SBRC improves the detection and mitigation of anomalous samples, thereby reducing their disruptive influence on cluster formation. Comprehensive descriptions of both algorithms follow.

MBRC is conceptually derived from large-margin learning techniques [25]. It integrates the notion of cluster margin distance and employs this metric alongside the distance between a new sample and the respective subcluster centroid to guide subcluster allocation. Large-margin optimization has been shown to inherently suppress the effects of outliers and noisy observations. Additionally, it provides natural adaptability to situations involving class imbalance or asymmetric misclassification penalties.

SBRC leverages an anomaly detection threshold generated by the Riemannian potato algorithm [26] to determine subcluster membership, effectively filtering out disruptive abnormal samples. The Riemannian potato algorithm serves as a distance-based outlier identification technique capable of reliably separating normal from aberrant signals [27, 28]. Signals whose Riemannian distance from reference data exceeds the established threshold are classified as anomalous and excluded.

The present work proposes MBRC and SBRC as innovative solutions to advance the classification of lower-limb MI-EEG signals. Departing from standard Riemannian clustering practices, these methods integrate subcluster partitioning with two newly formulated clustering criteria. Validation was performed using one experimental dataset and one publicly available dataset, confirming the practical advantages of the proposed approaches.

Materials and Methods

Dataset description

The present study employed one online experimental dataset and one offline public dataset to assess the effectiveness of the proposed algorithms. The online experiment recruited 10 healthy participants (three females). Six of these individuals were engaging in a lower-limb MI experiment for the first time. Prior to participation, all subjects received a detailed explanation of the experimental procedures and provided written informed consent. The study protocol was approved by the ethics committee of Tianjin University. The offline dataset consisted of the Yi2014 dataset [29], which contains EEG recordings from 10 healthy subjects performing seven classes of motor imagery tasks in a seated position.

Experiment dataset

Ten healthy volunteers (four females and six males) took part in the experimental session. Five participants had no previous exposure to lower-limb motor imagery-based BCI paradigms. All experimental sessions were carried out in a quiet, dedicated BCI laboratory environment. During recordings, subjects were required to stand comfortably with their bodies relaxed while minimizing head and facial movements to reduce artifacts. Following each experimental block, participants were allowed to sit and rest until any fatigue was fully alleviated. The paradigms for the resting and lower-limb MI conditions are illustrated in **Figures 1a and 1b**, respectively.

At the start of each trial, a white fixation circle was displayed at the center of the screen for 2 seconds, permitting subjects to blink, swallow, or adjust their posture as needed. Subsequently, a red circle appeared at the center, signaling the imminent onset of the task. The resting condition was cued by a static standing image and lasted for 4 seconds, during which subjects were instructed to remain motionless while standing. The lower-limb MI task was cued by a slow-motion video depicting a leg-kick movement and also lasted for 4 seconds. During this interval, participants were asked to imagine performing the leg-kick action in synchrony while maintaining a standing posture. Each subject completed two experimental blocks, with each block containing 50 trials (25 resting trials and 25 lower-limb MI trials) presented in randomized order.

Raw EEG signals were recorded using a SynAmps2 system equipped with a 64-channel EEG quick-cap. Electrode placement followed the international 10/20 system. Twenty-five channels were selected for recording, as indicated by the shaded regions in **Figure 1c**. The reference electrode (REF) was positioned at the tip of the nose, and the ground electrode (GND) was placed at the center of the forehead. The raw EEG data were sampled at 1000 Hz, and a 50 Hz notch filter was applied during acquisition to eliminate power-line interference.

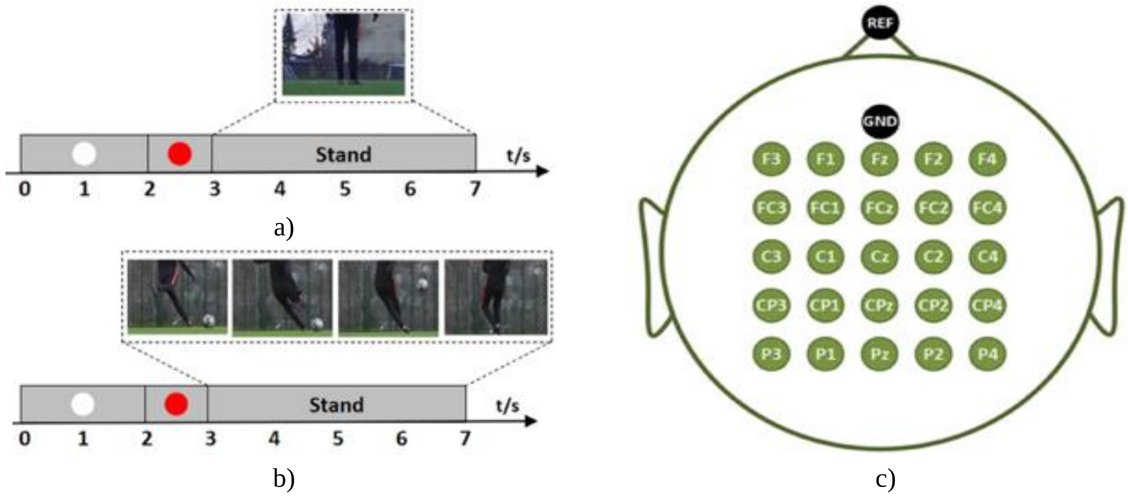

Figure 1. (a) Timing sequence of a resting trial in the experiment. A white circle was first presented for 2 s, during which the subject remained at rest. This was followed by the display of a red circle for 1 s to alert the subject to prepare for the upcoming task. From 3 s to 7 s, the subject performed the resting task while

viewing the static image. (b) Timing sequence of a lower-limb MI trial in the experiment. The sequence from 0 s to 3 s was identical to that of the resting trial. From 3 s to 7 s, subjects performed the lower-limb motor imagery task while viewing a video of a ball-kicking movement. (c) Electrode locations selected for the experiment.

Dataset Yi2014

The Yi2014 dataset served as an additional resource for validating the performance of the proposed approaches. This dataset includes EEG recordings collected from ten right-handed healthy individuals (seven females and three males, aged between 23 and 25 years). All participants were novices with no previous exposure to motor imagery-based BCI systems. Prior to the main recording sessions, they completed a one-week training period. Resting-state trials and double foot-lifting motor imagery trials were selected for analysis (80 trials per class per participant). Due to incomplete recordings from one subject, data from only nine participants were retained for the current investigation. The experimental paradigms corresponding to the resting and motor imagery conditions are presented in **Figures 2a and 2b**, respectively. EEG signals were originally acquired with a SynAmps2 amplifier and a 64-channel quick-cap at a sampling rate of 1000 Hz, with a bandpass filter applied between 0.5 and 100 Hz. Sixty channels were utilized in this study, as indicated in **Figure 2c**. The reference electrode (REF) was positioned at the tip of the nose, and the ground electrode (GND) was located at the center of the forehead.

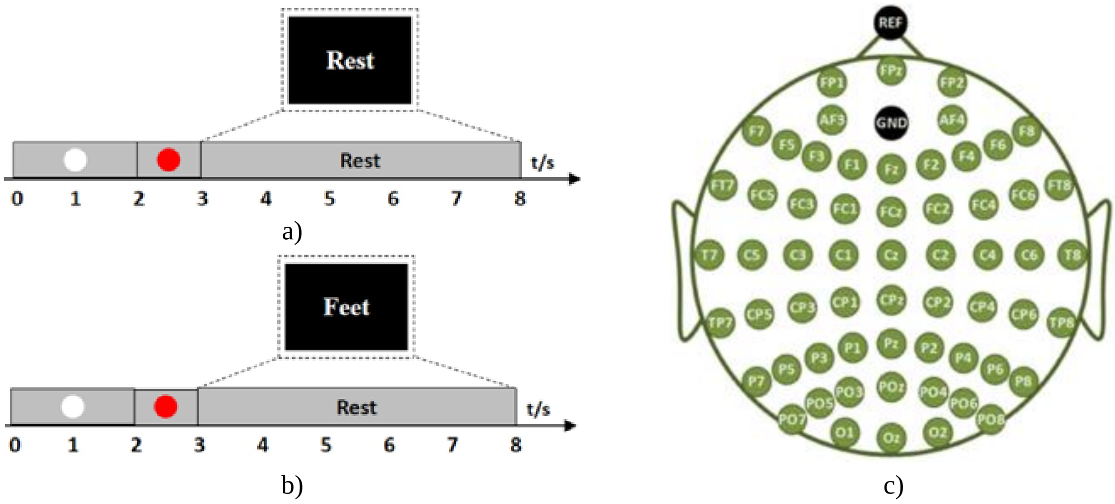

Figure 2. (a) Timing sequence of a resting trial from the Yi2014 dataset. The trial commenced with the presentation of a white circle for 2 s, during which the subject remained at rest. A red circle then appeared for 1 s to signal task preparation. From 3 s to 8 s, the subject performed the resting task. (b) Timing sequence of a lower-limb MI trial from the Yi2014 dataset. The initial segment from 0 s to 3 s followed the same structure as the resting trial. From 3 s to 8 s, subjects carried out the lower-limb motor imagery task. (c) Electrode montage selected for the Yi2014 dataset.

Preprocessing

EEG recordings underwent down-sampling to 200 Hz, followed by application of a 4–30 Hz bandpass filter. Data segments spanning 3 s to 7 s were subsequently extracted for analysis. To comprehensively assess the capabilities of the developed algorithms, training sets of progressively increasing size were utilized, with the unused portions serving as test data. In the case of the Yi2014 dataset, training sample sizes ranged from 10 to 150 trials, advancing in steps of 10. Each training-test configuration was repeated twenty times, and the resulting performance measures were averaged. Within each repetition, trial order was randomly permuted prior to selecting the required number of training samples, with all remaining trials assigned to the test set.

Comparative evaluations were conducted against several conventional techniques: CSP combined with support vector machine (SVM), power spectral density (PSD) paired with linear discriminant analysis (LDA), EEGNet, Riemannian minimum distance to mean (MDRM), and tangent space LDA (TSLDA). Classification outcomes from the Yi2014 dataset enabled the identification of an optimal data partitioning scheme for training. This scheme was subsequently adopted for the experimental dataset. Specifically, the initial 20 trials within each block were allocated to training, while the final 30 trials were reserved for testing. The identical set of algorithms and parameter configurations applied to the Yi2014 data was then used to conduct pseudo-online evaluations on the experimental recordings.

Riemannian geometric framework

Riemannian geometry constitutes a mathematical discipline concerned with the analysis of smooth, curved spaces that exhibit local Euclidean properties. With suitable transformations, such spaces can be modeled as Riemannian manifolds possessing associated tangent spaces [30]. This approach is valued for its straightforward implementation, resilience against disturbances, and effectiveness in transfer learning scenarios [31]. Within BCI research, an EEG signal is modeled as a point lying on a high-dimensional Riemannian manifold. The Riemannian distance separating two covariance matrices C_1 and C_2 is given by the expression:

$$\delta_R(C_1, C_2) = \left\| \mathrm{Log}\left(C_1^{-1/2} C_2 C_1^{-1/2} \right) \right\|_F = \left(\sum_{n=1}^{N} \log_2 \lambda_n \right)^{1/2} \quad (1)$$

where $\log(0)$ indicates the matrix logarithm operation, $\|0\|_F$ stands for the Frobenius norm, and λ_n refers to the *n*th eigenvalue of the matrix. $C_1^{-1/2} C_2 C_1^{-1/2}$.

Margin-Based Riemannian Clusters (MBRC)

MBRC partitions the training samples into several subclusters, each defined by four primary parameters listed in **Table 1**. A comprehensive overview of the MBRC training procedure is provided in **Figure 3**. Let $X \in R^{Nt \times C \times T}$ symbolize the collection of training covariance matrices and $y \in R^{Nt}$ represent the associated class labels. In this notation, N_t, C and T correspond to the total number of training trials, recording channels, and time points per trial, respectively. Furthermore, $S = \{S_1, \ldots, S_{Nt}\}$ designates the status indicator for each individual trial, while $Cl = \{Cl_1, \ldots, Cl_{Nc}\}$ serves as the status indicator for each class, with N_c denoting the overall number of classes.

Table 1. Parameters of the MBRC subcluster.

Parameter	Description
Ir	Represents the total number of sample covariance matrices included within the corresponding subcluster.
kr	Indicates the category assigned to the subcluster, with every sample covariance matrix in that subcluster belonging to the same class.
Mr	Denotes the Riemannian mean calculated from all sample covariance matrices contained in the subcluster.
br	Refers to the greatest Riemannian distance observed between any sample covariance matrix in the subcluster and its Riemannian mean, **Mr**.

Abbreviation: MBRC, Margin Based Riemannian Clusters.

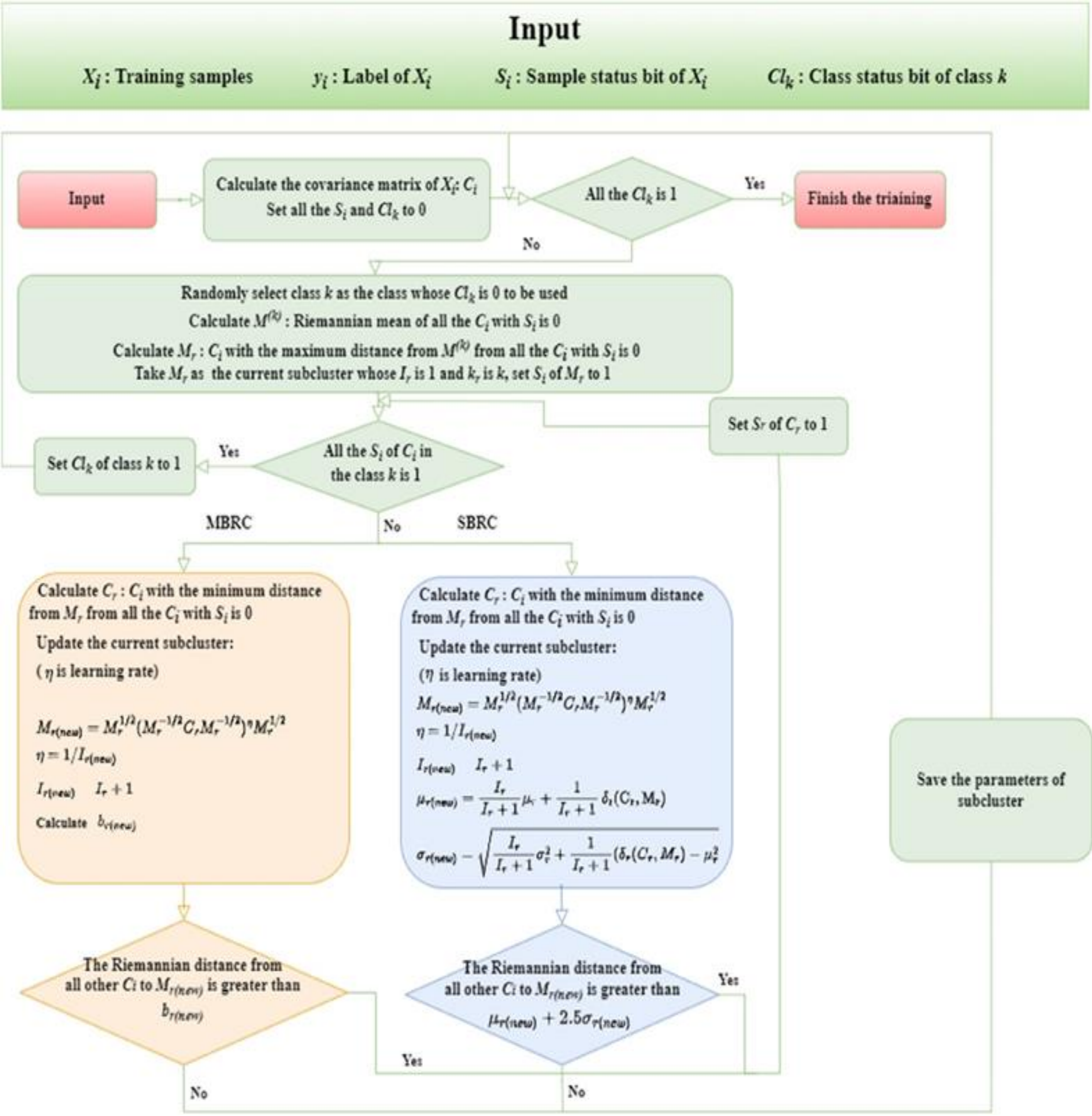

Figure 3. Detailed training workflow for MBRC and SBRC.

Green-highlighted steps are shared by both algorithms, orange-highlighted steps apply exclusively to MBRC, and blue-highlighted steps are unique to SBRC. MBRC: margin-based Riemannian clusters; SBRC: statistics-based Riemannian clusters.

Both sample status indicators and class status indicators are initialized at 0. For any given subcluster, the Riemannian mean $\boldsymbol{M_r}$ is computed from its member samples. This mean is then compared via Riemannian distances against other samples belonging to the same class to evaluate potential merging. When a new covariance matrix $\boldsymbol{M_r}$ joins the subcluster, the mean is refreshed iteratively via the relation:

$$\boldsymbol{M}_{r(\text{new})} = \boldsymbol{M}_r^{1/2}\left(\boldsymbol{M}_r^{-1/2}\boldsymbol{C}_r\boldsymbol{M}_r^{-1/2}\right)^{\eta}\boldsymbol{M}_r^{1/2} \tag{2}$$

in which $\boldsymbol{M}_{r(\text{new})}$ is the revised subcluster mean and η is the learning rate parameter. The value $\eta = 0$ leaves $\boldsymbol{M}_{r(\text{new})}$ identical to $\boldsymbol{M_r}$, whereas $\eta = 1$ sets $\boldsymbol{M}_{r(\text{new})}$ equal to $\boldsymbol{C_r}$. The updated sample count becomes $I_{r(\text{new})} = I_r+1$, and the learning rate is defined as $\eta = 1/I_{r(\text{new})}$. The updated intra-cluster boundary $b_{r(\text{new})}$ is subsequently determined. Should the Riemannian distances from all samples of differing classes to $\boldsymbol{M}_{r(\text{new})}$ surpass $b_{r(\text{new})}$, the relevant sample status indicator is changed to 1, and the refined subcluster parameters are preserved.

Should no additional samples sharing the class of $\boldsymbol{M_r}$ retain a status indicator of 0, the class status indicator for the present class k is updated to 1. The entire training procedure terminates when status indicators for every class reach 1.

This mechanism identifies the sample most distant from the subcluster mean and the nearest sample from other classes as boundary representatives. The Riemannian distance between these boundary samples and the subcluster mean quantifies the separation gap. Greater separation reduces generalization error relative to other classes.
For classification of new samples, MBRC evaluates Riemannian distances between the test covariance matrix and the means of all established subclusters. Assignment occurs to the subcluster yielding the minimal distance value.

Statistics-Based Riemannian Clusters (SBRC)

Following the principles of the Riemannian potato algorithm, the Riemannian mean M is first established from covariance matrices of normal baseline signals. The corresponding threshold th is derived through the subsequent relations:

$$\mu = \frac{1}{I}\sum_{i=1}^{I}\delta_R(\boldsymbol{C_i}, \boldsymbol{M}) \tag{3}$$

$$\sigma = \sqrt{\frac{1}{I}\sum_{i=1}^{I}\left(\delta_R(\boldsymbol{C_i}, \boldsymbol{M}) - \mu\right)^2} \tag{4}$$

$$th = \mu + 2.5\sigma \tag{5}$$

where I signifies the quantity of covariance matrices, μ expresses the mean distance of baseline matrices to M, and σ reflects the standard deviation of those distances [26].
SBRC accepts identical input data as MBRC. The defining parameters for each SBRC subcluster closely mirror those of MBRC and are presented in **Table 2**.

Table 2. Parameters of the SBRC subcluster.

Parameter	Description
Ir	The total count of sample covariance matrices that make up the corresponding subcluster.
kr	Specifies the class label of the subcluster, where every sample covariance matrix within the subcluster is assigned to the same class.
Mr	The Riemannian mean computed from all sample covariance matrices contained in the subcluster.
μr	The average Riemannian distance between each sample covariance matrix in the subcluster and the subcluster mean, **Mr**.
σr	The standard deviation of the Riemannian distances from each sample covariance matrix in the subcluster to the subcluster mean, **Mr**.

Abbreviation: SBRC, statistics based Riemannian clusters.

Analogous to MBRC, all sample and class status indicators begin at 0. The Riemannian mean $\boldsymbol{M_r}$ for samples within a subcluster is calculated and compared with other same-class samples to assess merging suitability. Upon integration of a new sample, the mean is revised using Equation (2). Once $\boldsymbol{M}_{r(\mathrm{new})}$ and $I_{r(\mathrm{new})}$ are obtained, the average intra-cluster distance μ_r and its standard deviation σ_r are refreshed according to Equations (6) and (7).

$$\mu_{r(\mathrm{new})} = \frac{I_r}{I_r+1}\mu_r + \frac{1}{I_r+1}\delta_R(\boldsymbol{C_r}, \boldsymbol{M_r}) \tag{6}$$

$$\sigma_{r(\mathrm{new})} = \sqrt{\frac{I_r}{I_r+1}\sigma_r^2 + \frac{1}{I_r+1}\left(\delta_R(\boldsymbol{C_r}, \boldsymbol{M_r}) - \mu_r\right)^2} \tag{7}$$

If Riemannian distances from covariance matrices of all other-class samples to $\boldsymbol{M}_{r(\mathrm{new})}$ exceed the threshold $\mu_{r(\mathrm{new})} + 2.5\sigma_{r(\mathrm{new})}$, the status indicator for $\boldsymbol{C_r}$ is switched from 0 to 1. The updated values $I_{r(\mathrm{new})}$, $\boldsymbol{M}_{r(\mathrm{new})}$, $\mu_{r(\mathrm{new})}$ and $\sigma_{r(\mathrm{new})}$ then become the current parameters. When no further same-class samples with status 0 remain relative to $\boldsymbol{M_r}$, the class status indicator for class k is set to 1. Training concludes as soon as all classes possess status indicators of 1.
During testing, SBRC assigns an unlabeled sample to a subcluster by calculating Riemannian distances to all subcluster means. The sample is allocated to the subcluster with the smallest distance.

Contrast Baseline Algorithm

CSP

The Common Spatial Pattern (CSP) algorithm represents one of the most extensively employed approaches for motor imagery (MI) electroencephalography (EEG) feature extraction in binary classification tasks. Its core principle involves identifying an optimal set of spatial filters through matrix diagonalization, thereby maximizing the variance disparity between the two signal classes and yielding highly discriminative feature vectors [32]. The associated objective function is expressed in the following equation:

$$\hat{w} = \underset{w}{\operatorname{argmax}} \frac{w^T \overline{R}_1 w}{w^T \overline{R}_2 w} \tag{8}$$

where $\bar{R}_1$ and $\bar{R}_2$ are the covariance matrix means of the two classes of data respectively.
A spatial filter $= [w_1, \ldots, w_{2m}]$ is derived from the eigenvectors w associated with the m largest and smallest values of the objective function. The original EEG signals are subsequently projected onto an uncorrelated vector space as follows:

$$Z_i = W^T X_i \tag{9}$$

The CSP features are then computed according to:

$$\sigma^i = \log\left(\frac{\operatorname{var}(Z_i)}{\sum_{i=1}^{2m} \operatorname{var}(Z_i)}\right), i = 1, 2, \ldots, 2m \tag{10}$$

where $\log(0)$ denotes the logarithmic transformation. In the present study, the number of CSP filters was configured to 2 (i.e., m = 1).

EEGNet

EEGNet constitutes a neural network architecture designed to extract spatiotemporal features directly from raw EEG signals [33]. The model acquires frequency-selective filters via a temporal convolution layer, acquires frequency-specific spatial filters through a depthwise convolution layer, and integrates features by means of a separable convolution layer that combines different convolution operations. In contrast to conventional algorithms, EEGNet demonstrates applicability across a broad spectrum of brain-computer interface (BCI) paradigms, with its learned features offering neurophysiological interpretability.
In this investigation, the EEGNet model was configured with 8 temporal filters, a kernel length equal to half the sampling rate of the signal (100 Hz), 2 spatial filters, a dropout rate of 0.5, a batch size of 32, and 200 training epochs.

ATCNet

The attention-based temporal convolutional network (ATCNet) employs a suite of advanced techniques to enhance MI classification performance while maintaining a relatively compact parameter count [34]. ATCNet integrates principled machine learning design to construct a domain-specific deep learning architecture characterized by interpretable and explainable features. It incorporates multi-head self-attention mechanisms to emphasize the most informative components within MI-EEG signals, temporal convolutional layers to capture high-level temporal patterns, and convolutional sliding-window strategies to efficiently augment the MI-EEG dataset.
In the current study, the learning rate was set to 0.0009, the batch size to 64, and the number of training epochs to 200.

BaseNet

BaseNet provides a framework for investigating the influence of channel attention mechanisms on the decoding of EEG motor imagery signals [35]. Through systematic evaluation of multiple attention modules, the framework elucidates how various attention strategies can improve decoding precision and elevate the overall efficacy of

EEG-based motor imagery classification. This analysis establishes a robust benchmark for evaluating attention-enhanced methodologies in EEG decoding applications.
In this study, the CATLite attention module—which exhibited superior performance in the referenced work [35]—was integrated with the baseline algorithm.

MDRM

MDRM operates within a Riemannian geometry framework and serves as a standard approach for the recognition of MI EEG signals. This algorithm exhibits notable effectiveness under the Riemannian manifold setting and delivers accuracy levels on par with conventional techniques across several public MI datasets [22]. It determines the Riemannian means of covariance matrices corresponding to each class and classifies an unknown covariance matrix according to its proximity to the nearest class mean. The Riemannian means are obtained via the following formulation:

$$\boldsymbol{M} = \underset{\boldsymbol{C} \in \mathbf{SPD}}{\mathbf{argmin}} \sum_{\mathbf{i}=1}^{I} \delta_R^2(\boldsymbol{C}, \boldsymbol{C}_i) \tag{11}$$

where I is the number of covariance matrices and SPD is the set of all symmetric positive definite matrices of the same dimension as the covariance matrix.

Statistical analysis

To assess potential significant differences in classification accuracy among MBRC, SBRC, and the competing algorithms, paired t-tests were applied to derive p-values for pairwise comparisons. All resulting p-values then underwent false discovery rate (FDR) correction to minimize the likelihood of false positive findings.

Results and Discussion

Visualization results

To gain a clear visual insight into the behavior of the proposed methods, feature distributions from both the newly developed algorithms and the baseline approaches were examined. Dimensionality reduction of the high-dimensional feature sets was performed using t-SNE [34]. Feature distributions were generated using 80 training samples, with the projection of an independent set of 80 samples displayed for evaluation. **Figure 4** depicts the feature distribution for subject 2 in the Yi2014 dataset. Individual points correspond to single samples, where orange indicates foot motor imagery tasks and blue represents rest states. **Figures 4a–4g** illustrate the feature distributions produced by the various algorithms, with EEGNet chosen to represent the deep learning category. The visualizations indicate that the proposed algorithms yield improved class separability relative to the baselines. Although the general separation pattern is akin to that of MDRM, the new methods demonstrate superior management of samples near decision boundaries. **Figures 4h and 4i** show the subcluster divisions produced by MBRC and SBRC, respectively, with distinct marker shapes identifying different subclusters. Samples of the same class are distributed across multiple subclusters, and instances within each subcluster exhibit greater proximity to one another.

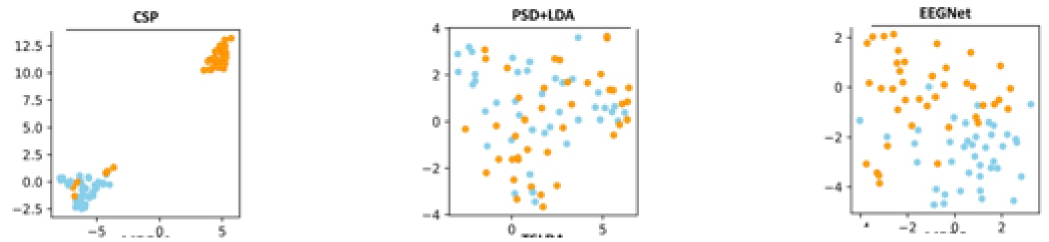

a) b) c)

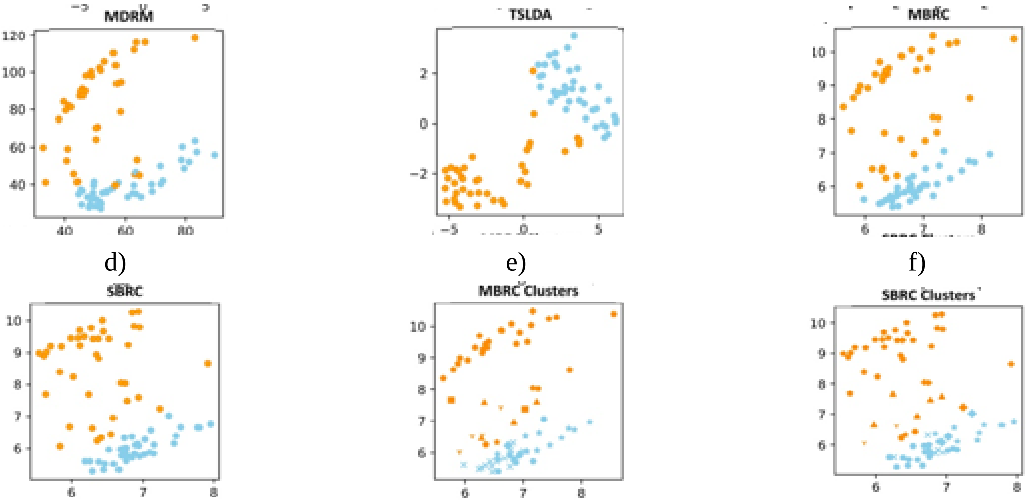

d) e) f)
g) h) i)

Figure 4. Visualization results for subject 2. Orange dots represent samples corresponding to foot tasks, while blue dots represent rest tasks. (a) Visualization results obtained with CSP. (b) Visualization results obtained with PSD + LDA. (c) Visualization results obtained with EEGNet. (d) Visualization results obtained with MDRM. (e) Visualization results obtained with TSLDA. (f) Visualization results obtained with margin based Riemannian clusters (MBRC). (g) Visualization results obtained with statistics based Riemannian clusters (SBRC). (h) Subcluster partitioning for MBRC. Different marker shapes indicate different subclusters. (i) Subcluster partitioning for SBRC. Different marker shapes indicate different subclusters.

Quantitative evaluation of the clustering effectiveness of the proposed MBRC and SBRC algorithms was conducted using two standard metrics: the Silhouette Score and the Cluster Separation Index. Mean values across subjects are summarized in **Table 3**. MDRM recorded the highest Silhouette Score (0.553) and Cluster Separation Index (0.713), signifying the strongest clustering quality overall. The proposed MBRC nevertheless performed strongly, attaining a Silhouette Score of 0.528 and a Cluster Separation Index of 0.704, which reflects effective cluster delineation. SBRC produced closely aligned outcomes, with a Silhouette Score of 0.531 and a Cluster Separation Index of 0.696.

Table 3. Average silhouette scores and cluster separation indices for MDRM, MBRC, and SBRC.

Evaluation Metric	MDRM	MBRC	SBRC
Silhouette coefficient	0.553	0.528	0.531
Cluster separation index	0.713	0.704	0.696

Abbreviations: MBRC, margin based Riemannian clusters; SBRC, statistics based Riemannian clusters.

Results on the Yi2014 dataset

Figure 5 presents the mean classification accuracy achieved by seven algorithms—CSP + SVM, PSD + LDA, EEGNet, ATCNet, BaseNet, MDRM, TSLDA, MBRC, and SBRC—across different training sample sizes. To examine whether meaningful differences in performance existed between MBRC, SBRC, and the remaining algorithms at various training sizes, paired t-tests were carried out on all training conditions, with FDR correction subsequently applied to the obtained p-values. The corresponding statistical results appear in **Figures 6 and 7**.

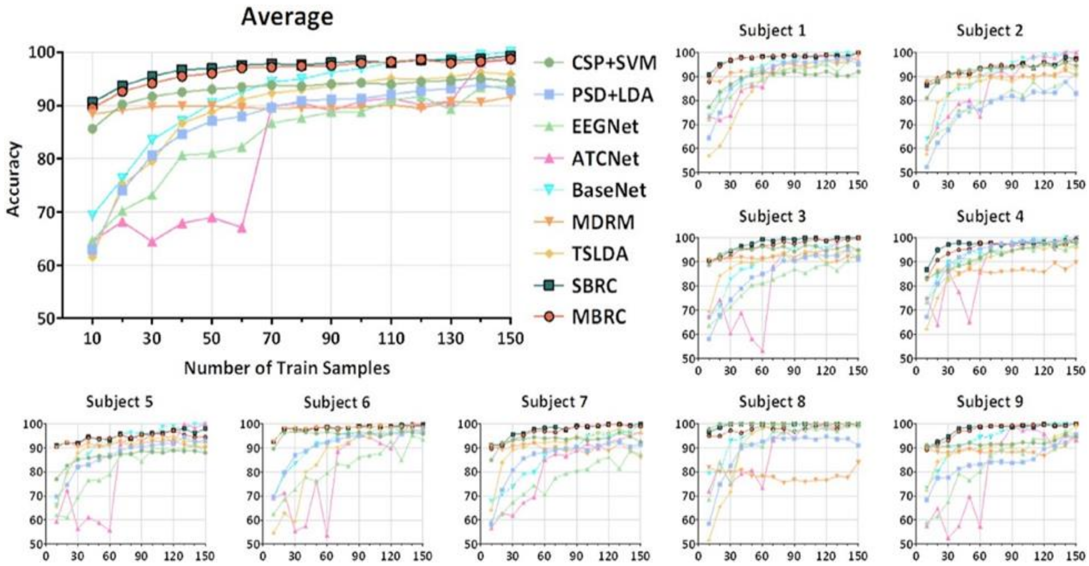

Figure 5. Classification accuracy attained by the proposed and baseline algorithms for varying numbers of training samples.

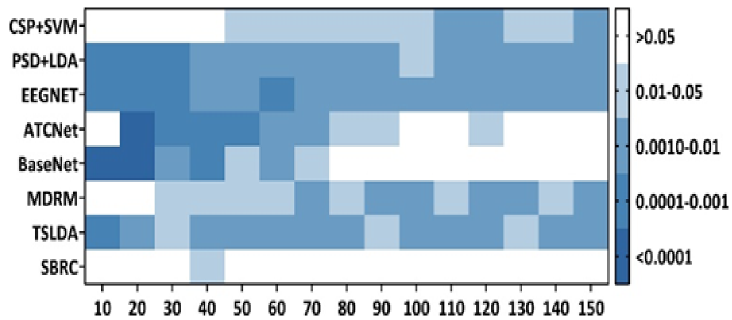

Figure 6. Statistically significant differences in classification accuracy between MBRC and the other algorithms across different training sample sizes. MBRC, margin based Riemannian clusters.

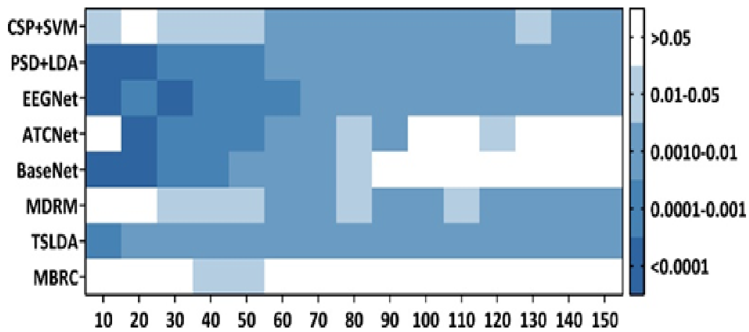

Figure 7. Statistically significant differences in classification accuracy between SBRC and the other algorithms across different training sample sizes. SBRC, statistics based Riemannian clusters.

With 10 training samples and 150 test samples, the average classification accuracies for CSP + SVM, PSD + LDA, EEGNet, ATCNet, BaseNet, MDRM, TSLDA, MBRC, and SBRC were 85.63 ± 6.41%, 62.95 ± 5.95%, 64.71 ± 5.04%, 64.43 ± 7.80%, 69.37 ± 6.10%, 88.36 ± 3.54%, 61.6 ± 6.54%, 89.52 ± 3.15%, and 90.62 ± 2.85%, respectively. Under these conditions, MBRC ranked second in average accuracy, while SBRC achieved the highest value.

At a training size of 10 samples, PSD + LDA, EEGNet, ATCNet, BaseNet, and TSLDA produced average accuracies below 70%, whereas the other algorithms surpassed 85%. Accuracy for both MBRC and SBRC rose steadily with increasing training data. As an illustration, when training samples grew from 30 to 150, MBRC accuracy advanced from 94.18 ± 2.37% to a peak of 98.72 ± 1.73%, and SBRC accuracy improved from 95.48 ± 2.82% to 99.33 ± 0.91%. The most favorable training configuration occurred when the training portion constituted 0.4 of the total data (equivalent to 60 trials). Additional training data beyond this threshold produced only negligible further improvements in accuracy. This outcome establishes an effective data allocation strategy for experimental dataset processing.

Table 4 details the pseudo-online execution time required to process one block per subject. As anticipated, deep learning models demanded considerably greater computational time. Although MBRC and SBRC exhibited modestly elevated runtimes compared with other methods, their processing remained near 0.1 s. This limited additional cost is deemed acceptable considering the substantial gains in classification performance delivered by these approaches.

Table 4. Runtime of all algorithms.

	CSP + SVM	PSD + LDA	EEGNet	ATCNet	BaseNet	MDRM	TSLDA	MBRC	SBRC
Runtime(s)	0.003	0.234	6.4	26.075	31.393	0.053	0.031	0.145	0.112

Results from the experimental dataset

To facilitate a detailed evaluation of multiple algorithms on an online experimental dataset, pseudo-online classification was conducted. The classification methods and their associated parameters in the online experiment—including frequency bands and sampling rate—were aligned with those used for the Yi2014 dataset. Analysis of the Yi2014 dataset revealed that optimal classification performance occurred when the training data proportion reached 0.4 of the total dataset. This ratio was therefore maintained for the current online experiment. For each block, the first 20 trials were treated as offline data and the following 30 trials as online data. Although only a single model (from MDRM, MBRC, or SBRC) was applied during each block, the complete dataset was preserved. This allowed the first 20 trials per round to serve as the training set and the remaining 30 trials as the test set, effectively replicating the online deployment conditions of the models used in the experiment.

Figure 8 presents the average accuracy rates, and **Table 5** provides the subject-specific classification accuracy details. The findings show that diminished intra-class homogeneity in the data caused a reduction in the classification performance of both MBRC and SBRC. Even so, both algorithms still outperformed the baseline approaches. MBRC recorded an average accuracy of 71.29%, while SBRC reached 73.12%. Notable differences were detected between ATCNet and the two newly developed algorithms. It appears that ATCNet struggled to achieve reliable classification due to its limited effectiveness during online testing. Unlike the results observed with the Yi2014 dataset, only CSP + SVM, EEGNet, and SBRC displayed statistically significant differences ($p < 0.05$).

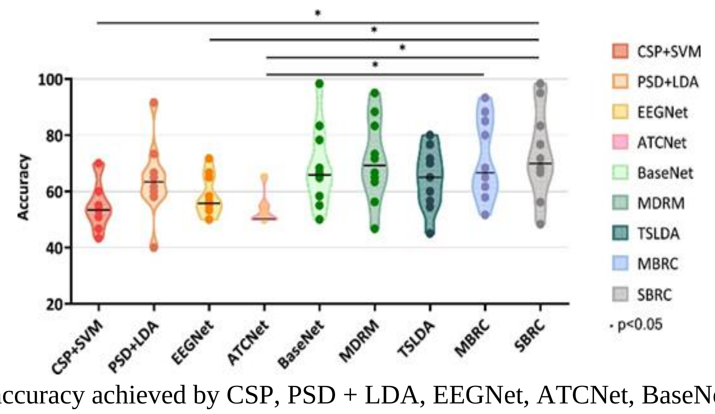

Figure 8. Average accuracy achieved by CSP, PSD + LDA, EEGNet, ATCNet, BaseNet, MDRM, TSLDA, MBRC, and SBRC across the dataset experiments. MBRC, margin-based Riemannian clusters; SBRC, statistics-based Riemannian clusters.

Table 5. Detailed classification accuracy for individual subjects.

Subject	CSP + SVM	PSD + LDA	EEGNet	ATCNet	BaseNet	MDRM	TSLDA	MBRC	SBRC
S1	53.333	66.667	71.667	50	68.33	95	80	88.333	95
S2	70	65	65	50	78.33	83.333	71.667	80	83.333

S3	53.333	66.667	50	50	58.33	63.333	56.667	65	66.667
S4	70	73.333	55	55	83.33	73.333	76.667	85	76.667
S5	43.333	91.667	50	65	98.33	88.333	65	93.333	98.333
S6	60	61.667	53.333	50	65	71.667	60	61.667	71.667
S7	46.667	58.333	66.667	50	66.67	66.667	70	68.333	66.667
S8	55	60	55	50	55	65	65	61.667	68.333
S9	50.924	58.067	56.343	52.65	64.84	56.281	54.372	57.882	56.158
S10	53.333	40	58.333	55	50	46.667	45	51.667	48.333
Mean	55.592	64.14	58.134	52.765	68.817	70.961	64.437	71.288	**73.116**
Std	8.832	13.048	7.313	4.779	14.386	14.745	10.723	14.293	15.782

Note: The bold values represent the maximum accuracy scores achieved among all compared algorithms.

Motor imagery (MI) brain-computer interfaces (BCIs) targeting the lower limbs hold significant promise for stroke rehabilitation. However, accurate classification remains difficult because of abundant artifacts in the signals. To address this, two innovative Riemannian clustering-based classification techniques were introduced, one utilizing boundary points and the other employing the Riemannian potato.

Figure 4 depicts the feature space distributions for both the proposed methods and the baseline algorithms. MBRC and SBRC exhibited clearer and more effective feature separation than the baseline techniques. Their classification behavior was comparable to that of MDRM, given that all three approaches operate through Riemannian distance measures within a clustering paradigm. Nevertheless, MBRC and SBRC handled class boundaries more effectively than MDRM, producing sharper distinctions between the two sample classes. This advantage stems from their ability to process boundary points with greater precision. By subdividing each class into several subclusters, the methods create multiple subcluster centers. This structure improves cohesion among samples of the same class and allows more adaptable boundary definitions.

Table 3 reveals that MDRM obtained the highest Silhouette Score (0.553) and Cluster Separation Index (0.713). These metrics indicate that MDRM provided the most balanced clustering quality in terms of both within-cluster compactness and between-cluster distinctness. The proposed MBRC algorithm performed strongly in comparison, attaining a Silhouette Score of 0.528 and a Cluster Separation Index of 0.704. Although its Silhouette Score was marginally below that of MDRM, MBRC's Cluster Separation Index was nearly identical, reflecting excellent inter-cluster separation capability. SBRC achieved a Silhouette Score of 0.531 and a Cluster Separation Index of 0.696, showing performance on par with MBRC. While SBRC fell slightly short of MDRM in cluster separation, it offered a well-balanced profile overall. Importantly, standard clustering indices may not adequately reflect the unique difficulties inherent in EEG data, including low signal amplitude and non-stationary characteristics. Despite similar clustering metrics, the proposed algorithms delivered higher classification accuracy than MDRM, suggesting they are better equipped to manage these EEG-specific issues.

Figure 5 illustrates that the proposed algorithms consistently produced superior accuracy compared with most baseline methods across different training sample sizes, except for BaseNet. With very limited training data (specifically 10 samples), MBRC and SBRC both surpassed 85% accuracy. This demonstrates their enhanced robustness relative to competing approaches. In contrast, PSD + LDA, EEGNet, ATCNet, BaseNet, and TSLDA showed weak results. The underlying causes likely include the challenges faced by deep learning models (EEGNet, ATCNet, and BaseNet) in learning meaningful features from scarce data, as well as the difficulty of LDA-based methods (in PSD + LDA and TSLDA) in determining an effective projection that accommodates all samples using only individual sample statistics. Conversely, the SVM classifier in CSP + SVM depends on a limited set of support vectors and avoids reliance on global sample statistics such as means or variances. MDRM, MBRC, and SBRC benefit from the inherent stability of Riemannian means. Consequently, these four algorithms maintained strong performance. With small sample sizes, however, MBRC and SBRC may not have formed enough subclusters, indicating potential for further accuracy gains.

As training sample size increased, MBRC and SBRC received more complete training and successfully identified a sufficient number of subclusters, leading to progressive improvements in accuracy.

Figures 6 and 7 display the p-values for comparisons between the proposed algorithms and the other methods. FDR correction was applied to control the false positive rate while preserving statistical power. The figures indicate no significant differences between MBRC and SBRC in the majority of cases (except at training set sizes of 40 and 50). Due to the FDR adjustment, the exact pattern of significance between MBRC and SBRC varies slightly between the two figures. The lack of significant difference likely arises because the core algorithmic structures are nearly identical, with only the decision criteria differing. This highlights that the overall framework exerts a dominant influence, whereas modifications to the criterion produce relatively minor effects. When integrated with the online experiment outcomes shown in **Figure 8**, the results reveal a significant difference between SBRC and MDRM (absent for MBRC), with SBRC attaining the highest overall accuracy. These findings confirm the strong performance of SBRC under online conditions.

We acknowledge that EEG signals exhibit substantial inter-subject variability, especially during motor imagery (MI) tasks, where individual neural response patterns can differ markedly. This variability may affect both classification accuracy and the generalizability of findings. Given the modest sample size of the present study and the potential influence of factors such as gender and personal EEG characteristics, a comprehensive examination of inter-subject variability was not performed. Although the proposed algorithms demonstrated encouraging group-level classification accuracy, we recognize that individual differences may impact their precision in specific cases. Nonetheless, the strong group-level performance highlights the potential utility of these methods.

Although the outcomes on both experimental and public datasets are encouraging, clinical validation through pilot studies or trials with stroke patients would offer more robust evidence regarding the algorithms' practical applicability in real-world scenarios. Future research should therefore prioritize evaluation of the proposed approach in actual clinical environments to confirm its suitability for stroke rehabilitation. In the current study, data were collected from a total of 9 subjects. Owing to this limited sample size, subsequent investigations could recruit a larger cohort, encompassing additional healthy participants as well as individuals with lower limb functional impairment. Such expansion would also enable comparative analyses of the proposed algorithms across diverse subject groups, thereby clarifying their effectiveness in patients with lower limb deficits.

To better address the requirements of stroke patients, particularly for extended rehabilitation training and real-time monitoring, the integration of wearable EEG devices is crucial [36-39]. In comparison with the elaborate setups typical of traditional laboratory environments, wearable systems reduce usage barriers for patients and facilitate wider deployment of brain-computer interface technology in domestic and rehabilitation settings. This shift enhances clinical adaptability and practical value. Accordingly, future studies will include clinical trials employing portable wearable EEG devices.

Conclusion

The present study introduces two novel Riemannian manifold clustering algorithms—MBRC and SBRC—for the classification of lower limb MI signals. Relative to conventional approaches, MBRC and SBRC deliver superior classification performance and demonstrate enhanced robustness under small-sample conditions. Results obtained from both the experimental dataset and the publicly available Yi2014 dataset confirm the viability of the proposed MBRC and SBRC methods. Overall, MBRC and SBRC represent promising techniques for improving the classification accuracy of MI EEG signals, with significant potential to advance the development of lower limb MI BCI systems.

Acknowledgments: None

Conflict of Interest: None

Financial Support: None

Ethics Statement: None

References

1. Katan M, Luft A. Global burden of stroke. Semin Neurol. 2018;38(2):208-11.
2. Kraus D, Naros G, Bauer R, Leão MT, Ziemann U, Gharabaghi A. Brain–robot interface driven plasticity: Distributed modulation of corticospinal excitability. Neuroimage. 2016;125:522-32.
3. Wolpaw JR, Wolpaw EW. Brain-computer interfaces: Principles and practice. In: Wolpaw JR, Wolpaw EW, editors. Brain-computer interfaces: Principles and practice. Oxford University Press; 2012. p. 3-12.

4. Mak JN, Arbel Y, Minett JW, McCane LM, Yuksel B, Ryan D, et al. Optimizing the P300-based brain–computer interface: Current status, limitations and future directions. J Neural Eng. 2011;8:025003.
5. Zhang Y, Xie SQ, Wang H, Zhang Z. Data analytics in steady-state visual evoked potential-based brain–computer interface: A review. IEEE Sens J. 2021;21(2):1124.
6. Wen H, Zhong Y, Yao L, Wang Y. Neural correlates of motor/tactile imagery and tactile sensation in a BCI paradigm: A high-density EEG source imaging study. Cyborg Bionic Syst. 2024;5:0118.
7. Padfield N, Zabalza J, Zhao H, Masero V, Ren J. EEG-based brain-computer interfaces using motor-imagery: Techniques and challenges. Sensors (Basel). 2019;19(6):1423.
8. Alder G, Signal N, Rashid U, Olsen S, Niazi IK, Taylor D. Intra- and inter-rater reliability of manual feature extraction methods in movement related cortical potential analysis. Sensors (Basel). 2020;20(8):2427.
9. Jochumsen M, Niazi IK. Detection and classification of single-trial movement-related cortical potentials associated with functional lower limb movements. J Neural Eng. 2020;17:035009.
10. Chaisaen R, Autthasan P, Mingchinda N, Leelaarporn P, Kunaseth N, Tammajarung S, et al. Decoding EEG rhythms during action observation, motor imagery, and execution for standing and sitting. IEEE Sens J. 2020;20:13776.
11. Yuan H, He B. Brain-computer interfaces using sensorimotor rhythms: Current state and future perspectives. IEEE Trans Biomed Eng. 2014;61(5):1425-35.
12. Blankertz B, Sannelli C, Halder S, Hammer EM, Kübler A, Müller KR, et al. Neurophysiological predictor of SMR-based BCI performance. Neuroimage. 2010;51(4):1303-9.
13. Singh A, Hussain AA, Lal S, Guesgen HW. A comprehensive review on critical issues and possible solutions of motor imagery based electroencephalography brain-computer interface. Sensors (Basel). 2021;21(6):2173.
14. Lotte F, Bougrain L, Cichocki A, Clerc M, Congedo M, Rakotomamonjy A, et al. A review of classification algorithms for EEG-based brain-computer interfaces: A 10 year update. J Neural Eng. 2018;15:031005.
15. Lotte F, Guan C. Regularizing common spatial patterns to improve BCI designs: Unified theory and new algorithms. IEEE Trans Biomed Eng. 2011;58:355.
16. Ang KK, Chin ZY, Zhang H, Guan C. Filter bank common spatial pattern (FBCSP) in brain-computer interface. In: 2008 IEEE International Joint Conference on Neural Networks (IEEE World Congress on Computational Intelligence). IEEE; 2008. p. 2390.
17. Park SH, Lee SG. Small sample setting and frequency band selection problem solving using subband regularized common spatial pattern. IEEE Sens J. 2017;17:2977.
18. Park SH, Lee D, Lee SG. Filter bank regularized common spatial pattern ensemble for small sample motor imagery classification. IEEE Trans Neural Syst Rehabil Eng. 2018;26(2):498-505.
19. Craik A, He Y, Contreras-Vidal JL. Deep learning for electroencephalogram (EEG) classification tasks: A review. J Neural Eng. 2019;16(3):031001.
20. Xie Y, Wang K, Meng J, Yue J, Meng L, Yi W, et al. Cross-dataset transfer learning for motor imagery signal classification via multi-task learning and pre-training. J Neural Eng. 2023;20(5):056037.
21. Congedo M, Barachant A, Bhatia R. Riemannian geometry for EEG-based brain-computer interfaces; A primer and a review. Brain-Computer Inter. 2017;4(3):155-74.
22. Barachant A, Bonnet S, Congedo M, Jutten C. Multiclass brain-computer interface classification by Riemannian geometry. IEEE Trans Biomed Eng. 2012;59(4):920.
23. Liu W, Guo C, Gao C. A cross-session motor imagery classification method based on Riemannian geometry and deep domain adaptation. Expert Syst Appl. 2024;237:121612.
24. Qian W, Zhou A. Analyzing popular clustering algorithms from different viewpoints. J Softw. 2002;13:1382.
25. Zhou ZH. Large margin distribution learning. In: Artificial neural networks in pattern recognition (ANNPR 2014). Cham: Springer; 2014. p. 1-11.
26. Barachant A, Andreev A, Congedo M. The Riemannian potato: An automatic and adaptive artifact detection method for online experiments using Riemannian geometry. 2013.
27. Duan X, Xie S, Xie X, Obermayer K, Cui Y, Wang Z. An online data visualization feedback protocol for motor imagery-based BCI training. Front Hum Neurosci. 2021;15:625983.
28. Huggins JE, Krusienski D, Vansteensel MJ, Valeriani D, Thelen A, Stavisky S, et al. Workshops of the eighth international brain-computer interface meeting: BCIs: The next frontier. Brain Comput Inter (Abingdon). 2022;9(2):69-101.

29. Yi W, Qiu S, Wang K, Qi H, Zhang L, Zhou P, et al. Evaluation of EEG oscillatory patterns and cognitive process during simple and compound limb motor imagery. PLoS One. 2014;9(12):e114853.
30. Yger F, Berar M, Lotte F. Riemannian approaches in brain-computer interfaces: A review. IEEE Trans Neural Syst Rehabil Eng. 2017;25(10):1753-62.
31. Pan L, Wang K, Xu L, Sun X, Yi W, Xu M, et al. Riemannian geometric and ensemble learning for decoding cross-session motor imagery electroencephalography signals. J Neural Eng. 2023;20(6):066011.
32. Ramoser H, Müller-Gerking J, Pfurtscheller G. Optimal spatial filtering of single trial EEG during imagined hand movement. IEEE Trans Rehabil Eng. 2000;8(4):441-6.
33. Lawhern VJ, Solon AJ, Waytowich NR, Gordon SM, Hung CP, Lance BJ. EEGNet: A compact convolutional neural network for EEG-based brain-computer interfaces. J Neural Eng. 2018;15(5):056013.
34. Altaheri H, Muhammad G, Alsulaiman M. Physics-informed attention temporal convolutional network for EEG-based motor imagery classification. IEEE Trans Ind Inf. 2023;19(2):2249-58.
35. Wimpff M, Gizzi L, Zerfowski J, Yang B. EEG motor imagery decoding: A framework for comparative analysis with channel attention mechanisms. J Neural Eng. 2024;21(3):036020.
36. Ding S, Saha T, Yin L, Liu R, Khan MI, Chang AY, et al. A fingertip-wearable microgrid system for autonomous energy management and metabolic monitoring. Nat Electron. 2024;7:788-98.
37. Wu P, Yiu CK, Huang X, Li J, Xu G, Gao Y, et al. Liquid metal-based strain-sensing glove for human-machine interaction. Soft Sci. 2023;3:35.
38. Chen C, Ding S, Wang J. Digital health for aging populations. Nat Med. 2023;29:1623-30.
39. Zhang M, Chi Z, Yang Z, Mohammed S, Huang J. Prescribed performance control of a human-following surveillance robot with incomplete observation. Cyborg Bionic Syst. 2024;5:0085.